SIAM J. APPL. MATH.
Vol. 71, No. 5, pp. 1780–1800

WAVEFORM DESIGN FOR SYNTHETIC-APERTURE RADAR IMAGING THROUGH DISPERSIVE MEDIA*

TROND VARSLOT†, J. HÉCTOR MORALES‡, AND MARGARET CHENEY§

Abstract. In this paper we analyze the problem of optimal waveform design for synthetic-aperture radar (SAR) imaging through a dispersive medium. We use a scalar model for wave propagation, together with the single-scattering approximation, and we assume that measurements are polluted with thermal noise whose statistics are known. For image formation, we use a filtered back-projection algorithm in which the filter is determined by knowledge of the power-spectral densities of the scene and noise. In this framework, we derive a waveform which is optimal in the sense of minimizing the mean-square-error of the reconstructed image. We show the results of simulations for the example of imaging point scatterers embedded in a certain dispersive background. We show that for low signal-to-noise ratios, the optimal waveform resembles what is known as a *precursor*: a wave that is generated from propagating ultrawideband waveforms through the medium.

Key words. synthetic aperture radar, waveform design, dispersive wave propagation, imaging, pulse-echo imaging

AMS subject classifications. 35Q60, 35R30, 78A46

DOI. 10.1137/100802438

1. Introduction.

A dispersive medium is one in which the speed of wave propagation depends on the frequency. All materials are dispersive to some extent [3]; however, for most current work on radar imaging, this effect has conveniently been neglected because (a) the dispersion is very weak in dry air, and (b) the frequency bands of most radar systems are not wide enough for dispersive effects to be important. However, it is well known [26] that range resolution is proportional to the bandwidth. As a consequence, high-resolution systems require broadband pulses, for which the issue of dispersion may become important.

Furthermore, an interesting phenomenon of wave propagation in dispersive media is the formation of *precursors*, which are transient waves with the remarkable property [21] that their amplitudes undergo only algebraic rather than exponential decay with propagation depth. Because of this property, it has been suggested [1, 4, 20] that precursors should be used for radar applications in dispersive media. This suggestion, however, has generated considerable controversy [18, 24], and the present paper provides one step in developing mathematical theory to settle the controversy.

The question of waveform design is a subtle one. In particular, it was shown in [6] and [7] that waveforms which maximize scattered energy are single-frequency waveforms. However, single-frequency waveforms have poor range resolution, which

*Received by the editors July 16, 2010; accepted for publication (in revised form) July 6, 2011; published electronically October 4, 2011. This work was supported by the Air Force Office of Scientific Research under the agreements FA9550-06-1-0017 and FA9550-09-1-0013. The U.S. Government retains a nonexclusive, royalty-free license to publish or reproduce the published form of this contribution, or allow others to do so, for U.S. Government purposes. Copyright is owned by SIAM to the extent not limited by these rights.

http://www.siam.org/journals/siap/71-5/80243.html

†Department of Applied Mathematics, Australian National University, Acton, 0200 ACT, Australia (trond@varslot.net).

‡Centro de Investigación en Matemáticas, A. C. Jalisco S/N, Col. Valenciana, 36240 Guanajuato, Gto, Mexico (moralesjh@cimat.mx).

§Department of Mathematical Sciences, Rensselaer Polytechnic Institute, Troy, NY 12180-3590 (cheney@rpi.edu).

shows that simply maximizing the received signal is not sufficient for producing a good synthetic-aperture radar (SAR) image. In order to find a waveform that produces an optimal image, it is necessary to include a measure of image quality in the optimization. Moreover, because the quality of the image formed from an attenuated signal is dependent on how the image formation process handles noise, it is important to develop an imaging theory that explicitly handles noise. This was carried out for SAR in [32] for the case of propagation in free space. The theory was extended to propagation through a dispersive medium in [8] and [30]. This paper builds on the foundation of [30] to develop a theory for the design of waveforms that are optimal for forming a SAR image through a dispersive medium. Our results suggest that under certain conditions, precursors may indeed be useful for SAR imaging.

This article is divided into seven sections. In section 2 we provide the mathematical model for scattering in a dispersive medium. We proceed to outline the filtered backprojection method in section 3. The theory for obtaining the optimal-waveform spectrum is presented in section 4; section 5 shows how to use the spectrum to obtain the optimal waveform itself. Numerical examples in section 6 illustrate the implementation of the algorithm. Some concluding remarks are given in section 7. Finally, Appendix A provides further details about the related developments in [30], and Appendix B provides some details for the dispersive medium model used in the simulations.

2. Wave propagation through a dispersive medium. In this section we give a brief review of the wave equations that govern the evolution of electromagnetic fields where weakly scattering objects are present in an otherwise homogeneous, dispersive medium. This serves the purpose of introducing our notation as well as giving an introduction to SAR imaging in a dispersive medium. For a more comprehensive treatment of the subject matter, the reader is encouraged to consult [8, 21, 30].

2.1. Maxwell's equations and constitutive relations. The propagation of electromagnetic waves is governed by the Maxwell equations, which are given in differential form by [14]:

$$\nabla \cdot \boldsymbol{D}(\mathbf{x}, t) = \rho(\mathbf{x}, t), \tag{2.1}$$

$$\nabla \cdot \boldsymbol{B}(\mathbf{x}, t) = 0, \tag{2.2}$$

$$\nabla \times \boldsymbol{E}(\mathbf{x}, t) = -\partial_t \boldsymbol{B}(\mathbf{x}, t), \tag{2.3}$$

$$\nabla \times \boldsymbol{H}(\mathbf{x}, t) = \partial_t \boldsymbol{D}(\mathbf{x}, t) + \boldsymbol{J}(\mathbf{x}, t). \tag{2.4}$$

Here, $\boldsymbol{D}$ is the electric displacement, $\boldsymbol{B}$ is the magnetic induction, $\boldsymbol{E}$ is the electric field, $\boldsymbol{H}$ is the magnetic field, ρ is the charge density, and $\boldsymbol{J}$ is the current density. The variable $\mathbf{x} = (x_1, x_2, x_3)^{\mathrm{T}} \in \mathbb{R}^3$ represents Cartesian coordinates, and $t \in \mathbb{R}$ is time. Finally, $\nabla\cdot$ denotes the divergence operator, and $\nabla\times$ denotes the curl operator.

In order to complete this set of equations, we will use the following constitutive relations [17, 25]:

$$\boldsymbol{D}(\mathbf{x}, t) = \int_0^\infty \varepsilon(\mathbf{x}, t')\boldsymbol{E}(\mathbf{x}, t - t')\mathrm{d}t' := (\varepsilon \underset{t}{*} \boldsymbol{E})(\mathbf{x}, t), \tag{2.5}$$

$$\boldsymbol{B}(\mathbf{x}, t) = \mu_0 \boldsymbol{H}(\mathbf{x}, t). \tag{2.6}$$

Here μ_0 denotes the free-space magnetic permeability. Since we integrate from 0 to ∞ in (2.5), the constitutive relation obeys causality; the dielectric response of the medium will be affected by the applied field $\boldsymbol{E}$ only at earlier times. We also note

that in turning (2.5) into a convolution, we have implicitly defined $\varepsilon(\mathbf{x}, t) := 0$ for $t < 0$.

We will frequently write quantities in the temporal frequency domain. As an example, we can express the electric field, $\boldsymbol{E}$, in terms of its Fourier transform, $\tilde{\boldsymbol{E}}(\mathbf{x}, \omega)$, as

$$\boldsymbol{E}(\mathbf{x}, t) = \frac{1}{2\pi} \int e^{-i\omega t} \tilde{\boldsymbol{E}}(\mathbf{x}, \omega) \mathrm{d}\omega. \tag{2.7}$$

The frequency-domain counterpart of the dielectric constitutive relation in (2.5) is then given by

$$\tilde{\boldsymbol{D}}(\mathbf{x}, \omega) = \epsilon(\mathbf{x}, \omega) \tilde{\boldsymbol{E}}(\mathbf{x}, \omega). \tag{2.8}$$

Here $\epsilon(\mathbf{x}, \omega)$ is the Fourier transform of $\varepsilon(\mathbf{x}, t)$.

2.2. Dispersion, wave numbers, and index of refraction. For a dispersive medium, the permittivity ϵ is frequency-dependent. Furthermore, in order to obey the causality requirement in our constitutive relation, ϵ must be complex-valued. In fact, if we let $\epsilon_R(\mathbf{x}, \omega) = \mathrm{Re}\{\epsilon(\mathbf{x}, \omega)\}$ and $\epsilon_I(\mathbf{x}, \omega) = \mathrm{Im}\{\epsilon(\mathbf{x}, \omega)\}$ denote the real and imaginary parts of $\epsilon(\mathbf{x}, \omega)$, respectively, then

$$\epsilon_R(\mathbf{x}, \omega) = \left[\mathcal{H}\epsilon_I\right](\mathbf{x}, \omega) := \mathrm{P.v.} \frac{1}{\pi} \int \frac{\epsilon_I(\mathbf{x}, \omega')}{\omega - \omega'} \mathrm{d}\omega', \tag{2.9}$$

where $\mathcal{H}$ is the Hilbert transform [22].

In terms of the relative permittivity of the medium $\epsilon_r = \epsilon/\epsilon_0$, the *index of refraction* is

$$n(\omega) := \sqrt{\epsilon_r(\omega)} \tag{2.10}$$

and is therefore also a complex-valued function; we denote the real and imaginary parts of n by n_R and n_I, respectively:

$$n(\omega) := n_R(\omega) + i\, n_I(\omega). \tag{2.11}$$

In order to avoid unphysical solutions, we choose the branch of the square root in (2.10) such that $\omega n_I(\omega)$ has positive sign. This branch corresponds to attenuation rather than amplification of the propagating electromagnetic waves.

From the index of refraction, we can define the wave number and the phase velocity. The (complex) *wave number* $k(\omega)$ is defined as

$$k(\omega) := \omega n(\omega)/c_0 = \omega\sqrt{\epsilon_r(\omega)}/c_0. \tag{2.12}$$

The *phase velocity* v_p is the speed at which the phase of any one frequency component propagates. It is

$$v_p(\omega) := \frac{c_0}{n_R(\omega)}. \tag{2.13}$$

Here $c_0 = 1/\sqrt{\mu_0\epsilon_0}$ is the speed of light in vacuum. See section 1.3 in [19] for a detailed discussion of the index of refraction.

2.3. The scalar wave model. To arrive at the wave equation for the electric field in a homogeneous dispersive medium, we use (2.5) and (2.6) to eliminate $\boldsymbol{D}$ and $\boldsymbol{B}$ in (2.3) and (2.4). Then we substitute the curl of (2.3) into (2.4), obtaining

$$\nabla \times \nabla \times \boldsymbol{E} = -\partial_t \mu_0 \boldsymbol{J} - \partial_t^2 (\mu_0 \varepsilon \underset{t}{*} \boldsymbol{E}). \tag{2.14}$$

We use the identity

$$\nabla \times \nabla \times \boldsymbol{E} = \nabla(\nabla \cdot \boldsymbol{E}) - \nabla^2 \boldsymbol{E} \tag{2.15}$$

to write (2.14) as

$$\nabla^2 \boldsymbol{E} - \partial_t^2 (\mu_0 \varepsilon \underset{t}{*} \boldsymbol{E}) = \nabla(\nabla \cdot \boldsymbol{E}) + \mu_0 \partial_t \boldsymbol{J}. \tag{2.16}$$

We denote the right side of (2.16) by $-\boldsymbol{J}_s$, which converts (2.16) into

$$\nabla^2 \boldsymbol{E} - \partial_t^2 (\mu_0 \varepsilon \underset{t}{*} \boldsymbol{E}) = -\boldsymbol{J}_s. \tag{2.17}$$

In a homogeneous material with no sources, $\nabla \cdot \boldsymbol{E} = 0$ and $\boldsymbol{J} = 0$, which implies that the source term $\boldsymbol{J}_s$ is nonzero only where sources or scatters are present. As a result, each component of the electric field satisfies a scalar wave equation of the form

$$\nabla^2 E - \partial_t^2 (c_0^{-2} \varepsilon_r \underset{t}{*} E) = -j_s. \tag{2.18}$$

Here j_s denotes one component of $\boldsymbol{J}$ in (2.17).

2.4. Scattering model. In this section we will state some underlying assumptions about the dispersive medium, which correspond to the situation shown in Figure 1. In essence, we consider a situation in which the radar pulse propagates through a known material, e.g., a forested area, for which we have an effective (homogeneous) propagation model. The pulse is then reflected off a nondispersive surface and then propagates back through the known material to the antenna.

The reflectivity of the surface is different at different points; this variation corresponds to different objects from which the radar energy reflects. Here we have

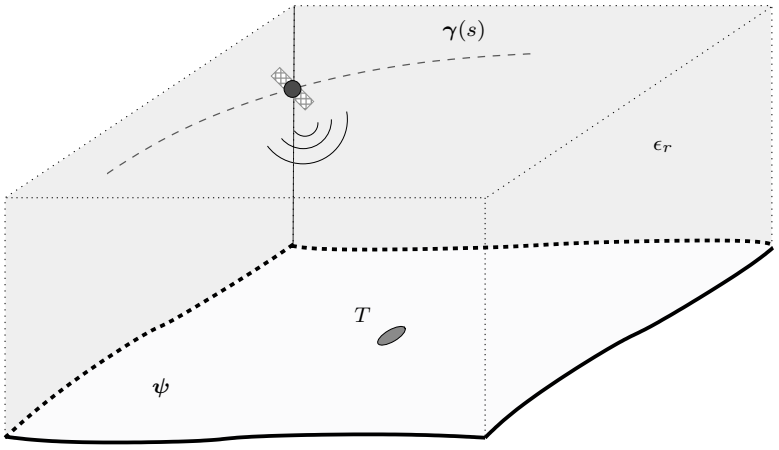

FIG. 1. *Background medium with a relative permittivity of ϵ_r, and a target T.*

effectively replaced the three-dimensional spatial configuration by a two-dimensional surface with varying reflectivity. The situation is analogous to forming an optical image of a two-dimensional photograph instead of the original three-dimensional scene that the photograph represents. We make this simplification to avoid dealing with the issue of how two-dimensional projections can be used to infer the shape of three-dimensional objects, which is a difficult problem in its own right.

To model the scattering, we use the following approach to arrive at a linear scattering model, which we use in subsequent sections.

In radar problems, the source $\boldsymbol{J}_s$ of (2.17) is a sum of two terms, $\boldsymbol{J}_s = \boldsymbol{J}^{\text{in}} + \boldsymbol{J}^{\text{sc}}$, where $\boldsymbol{J}^{\text{in}}$ corresponds to the effective current density on the transmitting antenna, and $\boldsymbol{J}^{\text{sc}}$ corresponds to currents induced on the the scattering object [5]. Fortunately, for our purposes it is not necessary to provide a detailed analysis of these currents on the target; for stationary objects consisting of linear materials, we assume that the interaction is linear and time-invariant, so that $\boldsymbol{J}^{\text{sc}}$ is related to $\boldsymbol{E}$ by a time-domain convolution $\boldsymbol{J}^{\text{sc}}(t,\boldsymbol{x}) = \int \boldsymbol{V}(t-t',\boldsymbol{x})\boldsymbol{E}(t',\boldsymbol{x})dt'$, where $\boldsymbol{V}$ is a matrix. For simplicity, we consider only one component of $\boldsymbol{V}$. We also use the *single-scattering* or *Born* approximation, i.e., we replace E by E^{in}:

$$j^{\text{sc}}(t,\boldsymbol{x}) = \int v(t-t',\boldsymbol{x})E^{\text{in}}(t',\boldsymbol{x})dt', \tag{2.19}$$

where $v(t,\boldsymbol{x})$ is called the *reflectivity function*.

Our precise assumptions about the nature of the background medium and about the reflectivity function are as follows.

ASSUMPTION 2.1 (scattering environment). *We assume the following:*

1. *The background medium (atmosphere) is homogeneous with known relative permittivity* $\varepsilon_r(t)$.
2. *The complex part of the index of refraction, as defined in* (2.11)*, is* $\mathcal{O}(1/\omega)$ *for large* ω [19]. *We note that high-frequency decay rates must be at least* ω^{-1} *for time-domain continuity* [14].
3. *Electromagnetic scattering occurs at the surface given by*

$$\mathbf{x} = \boldsymbol{\Psi}(x_1,x_2) := [x_1,x_2,\psi(x_1,x_2)]^{\mathrm{T}}, \tag{2.20}$$

   where the differentiable function $\psi : \mathbb{R}^2 \mapsto \mathbb{R}$ *is assumed to be known.*
4. *The target dispersion is known; in particular, when combined with* (2.20) *we assume that the reflectivity function can be written* $v(t,\boldsymbol{x}) = T(x_1,x_2)\delta(\mathbf{x} - \boldsymbol{\Psi}(x_1,x_2))\partial_t^2\delta(t)$.

We will use the term *target*, or *ground reflectivity function*, when we refer to T. The quantity T is what we want to reconstruct from the measured electromagnetic scattering (see Figure 1).

We consider the situation in which the transmitting and receiving antennas are isotropic, collocated, and follow a path γ in three-dimensional space, which we parametrize by s. Suppose at position $\gamma(s)$ the antenna transmits the waveform $p(t,s)$, whose temporal Fourier transform is $P(\omega,s)$. Then we have the following model for the observed scattering [30].

THEOREM 2.2. *Let* $\boldsymbol{y} := \{(y_1,y_2) \in \mathbb{R}^2\}$ *be a two-dimensional coordinate such that* $(y_1,y_2,\psi(y_1,y_2))$ *is a point on the surface* $\boldsymbol{\Psi}$*, and let* $\mathrm{d}\boldsymbol{y} = \mathrm{d}y_1\mathrm{d}y_2$ *be the two-dimensional surface measure. Under the single-scattering (Born) approximation, the scattered electric field* E^{sc} *is*

$$E^{\text{sc}}(\boldsymbol{\gamma}(s),t,s) = \iint \frac{e^{-i\omega(t-2n(\omega)|\mathbf{r}_{s,\boldsymbol{y}}|/c_0)}}{(16\pi^3)^2|\mathbf{r}_{s,\boldsymbol{y}}|^2}\omega^2 P(\omega,s)T(\boldsymbol{y})\Lambda(\boldsymbol{y})\mathrm{d}\omega\mathrm{d}\boldsymbol{y}, \tag{2.21}$$

where

$$\boldsymbol{r}_{s,\boldsymbol{y}} := \boldsymbol{\Psi}(\boldsymbol{y}) - \gamma(s), \tag{2.22}$$

and

$$\Lambda(\boldsymbol{y}) = \sqrt{1 + \left(\frac{\partial \psi}{\partial y_1}\right)^2 + \left(\frac{\partial \psi}{\partial y_2}\right)^2}. \tag{2.23}$$

The factor $\Lambda(\boldsymbol{y})$ accounts for the surface area on nonplanar topography. To keep notation simpler, we introduce a *modified target*

$$\tilde{T}(\boldsymbol{y}) := T(\boldsymbol{y})\Lambda(\boldsymbol{y}). \tag{2.24}$$

Furthermore, we will omit the tilde and write T. We should keep in mind, though, that formulas in the remainder of this paper are for the modified target. For flat topography there is no distinction.

Finally, we will include additive noise $\eta(t,s)$ in our data model:

$$d(t,s) := E^{\mathrm{sc}}(\gamma(s),t,s) + \eta(t,s). \tag{2.25}$$

3. Image formation. To form an image $I(\boldsymbol{z})$ (i.e., an estimate of $T(\boldsymbol{z})$), we apply to the noisy data (2.25) an operator B_Q of the form [30]

$$I(\boldsymbol{z}) = [B_Q d]\,(\boldsymbol{z}) := \iint\int e^{i\omega'\left(t - 2n_R(\omega')|\mathbf{r}_{s,\boldsymbol{z}}|/c_0\right)} Q(\omega', \boldsymbol{z}, s)\mathrm{d}\omega'\; d(t,s)\mathrm{d}t\mathrm{d}s. \tag{3.1}$$

The (explicit) phase of the integral operator B_Q involves only the real part $n_R(\omega)$. Because the real part corresponds to the correct propagation speed, this results in a backprojection method which places the scatterers at the correct spatial range. The choice of the filter Q is discussed below.

For a given flight-path γ and topography $\boldsymbol{\Psi}$, the set of target Fourier coefficients that can be measured by the sensor is known as the *data collection manifold* Ω_z (see [32] for details). Thus, under ideal noise-free conditions, the Plancherel theorem implies that the best L^2 representation of the target is

$$I_{\Omega_{\boldsymbol{z}}}(\boldsymbol{z}) := \int_{\Omega_{\boldsymbol{z}}}\int e^{i(\boldsymbol{y}-\boldsymbol{z})\cdot\boldsymbol{\xi}} T(\boldsymbol{y})\mathrm{d}\boldsymbol{y}\mathrm{d}\boldsymbol{\xi}. \tag{3.2}$$

Our aim here is to ensure that the image formation (3.1) provides a good image in the presence of noise. In determining the filter Q in the image formation algorithm, we are not as interested in the imaging performance for a specific target as we are in ensuring good performance over a whole class of targets. We therefore take a stochastic approach, in which we associate a probability measure with the class of possible targets. Based on how likely a given target is, we can say how likely a specific reconstruction is to yield a good image. Specifically, we minimize the mean-square-error (MSE) of the leading-order contributions of the resulting image. This is done by minimizing $\Delta(P,Q)$:

$$\Delta(P,Q) := \int \langle |I(\boldsymbol{z}) - I_{\Omega_{\boldsymbol{z}}}(\boldsymbol{z})|^2\rangle \mathrm{d}\boldsymbol{z}. \tag{3.3}$$

Here $\langle\cdot\rangle$ denotes the expectation operator. In [30] we analyzed the imaging operator B_Q under the following assumptions.

ASSUMPTION 3.1 (stochastic scattering). *The target T is a zero-mean wide-sense stationary second-order random field with known covariance function R_T:*

$$\langle T(\boldsymbol{y})\rangle = 0, \tag{3.4}$$

$$R_T(\boldsymbol{y}-\boldsymbol{y}') := \langle T(\boldsymbol{y})\overline{T(\boldsymbol{y}')}\rangle. \tag{3.5}$$

Here $\overline{T(\boldsymbol{y}')}$ is the complex conjugate of $T(\boldsymbol{y}')$. We define the target spectral density function S_T via the Fourier relation

$$R_T(\boldsymbol{y}-\boldsymbol{z}) = \int e^{-i(\boldsymbol{y}-\boldsymbol{z})\cdot\boldsymbol{\zeta}} S_T(\boldsymbol{\zeta})\mathrm{d}\boldsymbol{\zeta}. \tag{3.6}$$

Furthermore, the noise $\eta(t,s)$ is a zero-mean second-order stochastic process [15, 27] *which* (a) *is stationary in the fast-time variable t;* (b) *is statistically uncorrelated in the slow-time variable s; and* (c) *has a spectral density function S_η which we define through the relation*

$$\iint e^{i\omega t_1} e^{-i\omega' t_2} \langle\overline{\eta(t_1,s)}\eta(t_2,s')\rangle \mathrm{d}t_1\mathrm{d}t_2 = S_\eta(\omega,s)\delta(\omega-\omega')\delta(s-s'). \tag{3.7}$$

Here again the bar denotes complex conjugation. Finally, T and η are statistically independent:

$$\langle T(\boldsymbol{y})\overline{\eta(t,s)}\rangle = \langle T(\boldsymbol{y})\rangle\overline{\langle\eta(t,s)\rangle} = 0. \tag{3.8}$$

We define an attenuation factor A as follows:

$$A(\omega,s,\boldsymbol{z}) := \frac{\omega^2 e^{-2\omega n_I(\omega)|\mathbf{r}_{s,\boldsymbol{z}}|/c_0}}{(16\pi^3|\mathbf{r}_{s,\boldsymbol{z}}|)^2}. \tag{3.9}$$

It was shown in [30] (see summary in Appendix A) that the optimal reconstruction filter has the approximate form

$$Q^{\mathrm{opt}}(\omega,s,\boldsymbol{z}) = \frac{\overline{A(\omega,s,\boldsymbol{z})P(\omega,s)}}{|A(\omega,s,\boldsymbol{z})P(\omega,s)|^2 J(\omega,s,\boldsymbol{z}) + \sigma_{\eta T}(\omega,s,\boldsymbol{z})}, \tag{3.10}$$

where the (frequency-domain) noise-to-target ratio $\sigma_{\eta T}$ is defined as

$$\sigma_{\eta T}(\omega,s,\boldsymbol{z}) := S_\eta(\omega,s)/S_T(\omega,s,\boldsymbol{z}). \tag{3.11}$$

In [30] we showed that the *noise-to-target ratio* $\sigma_{\eta T}$ is closely related to the *signal-to-noise ratio* (SNR). In fact, the SNR is approximately $1/\sigma_{\eta T}$ times the square of the amplitude of a signal which is received after being scattered from a target with unit reflectivity. The important difference is that the SNR will depend on the distance from the target to the antenna, while the noise-to-target ratio does not.

The quantity $J = |\partial(\omega,s)/\partial\boldsymbol{\xi}|$ in (3.10) is known as the Beylkin determinant [2, 30], whose reciprocal is

$$\left|\frac{\partial\boldsymbol{\xi}}{\partial(\omega,s)}\right| = \left|\frac{4\omega}{v_p(\omega)v_g(\omega)}\det\begin{bmatrix}\widehat{\mathbf{r}_{s,\boldsymbol{z}}}\cdot\partial_{z_1}\boldsymbol{\Psi} & P_\perp\dot{\boldsymbol{\gamma}}(s)\cdot\partial_{z_1}\boldsymbol{\Psi}\\ \widehat{\mathbf{r}_{s,\boldsymbol{z}}}\cdot\partial_{z_2}\boldsymbol{\Psi} & P_\perp\dot{\boldsymbol{\gamma}}(s)\cdot\partial_{z_2}\boldsymbol{\Psi}\end{bmatrix}\right|. \tag{3.12}$$

Here $\widehat{\mathbf{r}}_{s,\boldsymbol{z}}$ denotes a unit vector in the direction of $\mathbf{r}_{s,\boldsymbol{z}}$, where the phase velocity v_p was defined in (2.13), and the *group velocity* v_g is defined as

$$v_g(\omega) := \frac{c_0}{n_R(\omega)+\omega\partial_\omega n_R(\omega)}. \tag{3.13}$$

We note that on the right side of (3.12), the determinant, which involves purely geometrical factors, is bounded above and below for typical systems; and for normal dispersion [12, 14] the group velocity is also bounded above and below.

With the filter (3.10), we obtain an approximation to the mean-square reconstruction error (3.3)

(3.14a)
$$\Delta(P,Q) \approx \int \left|Q(\omega,s,\boldsymbol{z})A(\omega,s,\boldsymbol{z})P(\omega,s)J(\omega,s,\boldsymbol{z})-1\right|^2 \frac{S_T(\,\boldsymbol{\xi}(\omega,s,\boldsymbol{z})\,)}{J(\omega,s,\boldsymbol{z})}\mathrm{d}\omega\mathrm{d}s\mathrm{d}\boldsymbol{z}$$

(3.14b)
$$+\int |Q(\omega,s,\boldsymbol{z})|^2 S_\eta(\omega,s)\mathrm{d}\omega\mathrm{d}s\mathrm{d}\boldsymbol{z}.$$

For the nondispersive case, we see that our reconstruction is identical to the variance-minimizing filter which was derived in [32], though the results therein were stated in terms of the image frequency variable ξ. Here, we have chosen to express the filter directly as a function of the data-collection variables (ω, s).

4. Waveform spectrum design. In section 3 we presented a filtered-back-projection-type reconstruction method that minimizes the MSE as defined in (3.3). We now address the problem of designing an accompanying waveform which will be optimal for use with this imaging filter.

Following [31], we insert (3.10) into (3.14a) to obtain

(4.1a)
$$\Delta(P,Q^{opt}) \approx \int \left|\frac{|A(\omega,s,\boldsymbol{y})P(\omega,s)|^2 J(\omega,s,\boldsymbol{z})}{|A(\omega,s,\boldsymbol{y})P(\omega,s)|^2 J(\omega,s,\boldsymbol{z})+\sigma_{\eta T}(\omega,s,\boldsymbol{z})}-1\right|^2 \frac{S_T(\omega,s,\boldsymbol{z})}{J(\omega,s,\boldsymbol{z})}\mathrm{d}\omega\mathrm{d}s\mathrm{d}\boldsymbol{z}$$

(4.1b)
$$+\int \frac{|A(\omega,s,\boldsymbol{y})P(\omega,s)|^2}{\left|\,|A(\omega,s,\boldsymbol{y})P(\omega,s)|^2 J(\omega,s,\boldsymbol{z})+\sigma_{\eta T}(\omega,s,\boldsymbol{z})\right|^2} S_\eta(\omega,s)\mathrm{d}\omega\mathrm{d}s\mathrm{d}\boldsymbol{z}.$$

This can be simplified as

(4.2a)
$$\Delta(P,Q^{opt}) \approx \int \frac{|\sigma_{\eta T}(\omega,s,\boldsymbol{z})|^2}{\left|\,|A(\omega,s,\boldsymbol{y})P(\omega,s)|^2 J(\omega,s,\boldsymbol{z})+\sigma_{\eta T}(\omega,s,\boldsymbol{z})\right|^2}\frac{S_T(\omega,s,\boldsymbol{z})}{J(\omega,s,\boldsymbol{z})}\mathrm{d}\omega\mathrm{d}s\mathrm{d}\boldsymbol{z}$$

(4.2b)
$$+\int \frac{|A(\omega,s,\boldsymbol{y})P(\omega,s)|^2}{\left|\,|A(\omega,s,\boldsymbol{y})P(\omega,s)|^2 J(\omega,s,\boldsymbol{z})+\sigma_{\eta T}(\omega,s,\boldsymbol{z})\right|^2} S_\eta(\omega,s)\mathrm{d}\omega\mathrm{d}s\mathrm{d}\boldsymbol{z}.$$

We can furthermore use the fact that the domain of integration is the same for both (4.2a) and (4.2b) to collect everything under the same integral:

$$\begin{aligned}\Delta(P,Q^{opt}) &\approx \int \left(\frac{|\sigma_{\eta T}(\omega,s,\boldsymbol{z})|^2 + |A(\omega,s,\boldsymbol{y})P(\omega,s)|^2\,\sigma_{\eta T}(\omega,s,\boldsymbol{z})\,J(\omega,s,\boldsymbol{z})}{\left|\,|A(\omega,s,\boldsymbol{y})P(\omega,s)|^2 J(\omega,s,\boldsymbol{z})+\sigma_{\eta T}(\omega,s,\boldsymbol{z})\right|^2}\right)\\ &\qquad\times \frac{S_T(\omega,s,\boldsymbol{z})}{J(\omega,s,\boldsymbol{z})}\,\mathrm{d}\omega\mathrm{d}s\mathrm{d}\boldsymbol{z}\\ &\approx \int \left(\frac{1}{|A(\omega,s,\boldsymbol{y})P(\omega,s)|^2 J(\omega,s,\boldsymbol{z})+\sigma_{\eta T}(\omega,s,\boldsymbol{z})}\right)\\ &\qquad\times \frac{S_T(\omega,s,\boldsymbol{z})\sigma_{\eta T}(\omega,s,\boldsymbol{z})}{J(\omega,s,\boldsymbol{z})}\mathrm{d}\omega\mathrm{d}s\mathrm{d}\boldsymbol{z}. \qquad (4.3)\end{aligned}$$

As we can see from (4.3), the resulting error depends on the choice of the transmit waveform spectrum, $|P(\omega, s)|^2$. We will therefore proceed to further minimize the reconstruction error by designing an optimal transmit waveform spectrum.

One immediate remark is that by increasing the transmit power, we can obtain an arbitrarily small MSE. However, in practice only limited power is available. A power constraint must therefore be imposed explicitly as part of the minimization. While typical systems employ the transmitted power at every point s on the trajectory, it turns out that this constraint is difficult to work with analytically. Consequently, we use instead the more flexible constraint that the total transmitted energy along the flight path is constant:

$$\int |P(\omega, s)|^2 \mathrm{d}\omega \, \mathrm{d}s = M, \tag{4.4}$$

where M is an arbitrary constant.

In order to determine the waveform spectrum which minimizes the asymptotic MSE, we employ the method of Lagrange multipliers. Let us therefore consider the functional $\Delta_\lambda(|P|^2)$:

$$\Delta_\lambda(|P|^2) = \Delta(P, Q^{opt}) + \lambda \left(\int |P(\omega, s)|^2 \mathrm{d}\omega \, \mathrm{d}s - M \right). \tag{4.5}$$

For notational convenience, let us also define $W(\omega, s) := |P(\omega, s)|^2$. Taking the variational derivative of $\Delta_\lambda(W)$ with respect to W, we obtain

$$\frac{\mathrm{d}}{\mathrm{d}\epsilon}\bigg|_{\epsilon=0} \Delta_\lambda(W + \epsilon W_\epsilon) = \int W_\epsilon \frac{-|A|^2 S_T \sigma_{\eta T}}{\left(|A|^2 J W + \sigma_{\eta T}\right)^2} \, \mathrm{d}\boldsymbol{z} \, \mathrm{d}\omega \, \mathrm{d}s + \lambda \int W_\epsilon \, \mathrm{d}\omega \, \mathrm{d}s. \tag{4.6}$$

For the optimal waveform, the right-hand side of (4.6) must be zero for all W_ϵ. We therefore must have

$$\int \frac{|A|^2 S_T \sigma_{\eta T}}{\left(|A|^2 J W + \sigma_{\eta T}\right)^2} \, \mathrm{d}\boldsymbol{z} = \lambda \tag{4.7}$$

for almost every (s, ω). If the power spectra S_T and S_η are continuous, (4.7) must hold for every (s, ω).

To solve (4.7), we use the fact that W is independent of $\boldsymbol{z}$ to rewrite (4.7) as

$$[\Phi(W)](\omega, s) = W(\omega, s), \tag{4.8}$$

where the functional $\Phi(W)$ is defined as

$$[\Phi(W)](\omega, s) := \begin{cases} \sqrt{\frac{1}{\lambda} \int \frac{S_T \sigma_{\eta T} A^2}{(A^2 J + \sigma_{\eta T}/W)^2} \, \mathrm{d}\boldsymbol{z}}, & W > 0, \\ 0, & W = 0. \end{cases} \tag{4.9}$$

Thus solving (4.7) is equivalent to finding a nonzero fixed point for the functional Φ.

THEOREM 4.1. *For any $M > 0$, the functional Φ has a nonzero fixed point satisfying $\int W(\omega, s) d\omega ds = M$.*

Proof. We observe that for each fixed (ω, s) and λ, $\Phi(W)$ has the following properties:

$$\Phi(W) \underset{W \to 0}{\to} W \sqrt{\frac{1}{\lambda} \int \frac{S_T A^2}{\sigma_{\eta T}} \, \mathrm{d}\boldsymbol{z}} \underset{W \to 0}{\to} 0, \tag{4.10}$$

$$\Phi(W) \underset{W \to \infty}{\to} \sqrt{\frac{1}{\lambda} \int \frac{S_T \sigma_{\eta T}}{A^2 J^2} \, \mathrm{d}\boldsymbol{z}}. \tag{4.11}$$

For each fixed (ω, s) and λ, we compare the two curves $w = \Phi(W)$ and $w = W$. Whenever λ is such that

$$\lambda < \int \frac{S_T A^2}{\sigma_{\eta T}} \, \mathrm{d}\boldsymbol{z}, \tag{4.12}$$

we find that for sufficiently small values of W, the curve $w = \Phi(W)$ lies above the line $w = W$, whereas for large W, the curve $w = \Phi(W)$ lies below the line $w = W$. Since for each (ω, s), $\Phi(W)$ is a continuous function of W, the curve must cross the line at some nonzero value of W. This means that for any (ω, s), we can find a parameter λ for which the equation $\Phi(W) = W$ has a nonzero solution. Furthermore, the function $\Phi(W)$ is a monotonically increasing function of $1/\lambda$; if W_1 is a fix-point for λ_1, and W_2 is a fix-point for λ_2, then $\lambda_2 < \lambda_1$ implies $W_2 > W_1$.

Now, by decreasing λ we will simultaneously expand the set of (s, ω) satisfying (4.12), and thus expand the set of (s, ω) for which we have a nonzero fix-point, and increase the fix-point value for each of those (s, ω). It is therefore clear that the transmit power M for the derived waveform also is a monotonically increasing function of $1/\lambda$, starting from $M = 0$ if λ is large enough so that (4.12) is never satisfied and thus no nonzero fix-points can be found for any (s, ω), and increasing to infinity as λ tends to 0. We can therefore obtain the optimal waveform spectrum by searching for a single parameter λ which results in a waveform spectrum which satisfies the power constraint (4.4). □

5. Getting the full waveform via spectral factorization. By solving (4.7), we have found the optimal transmit spectrum $|P(\omega, s)|^2$. In order to recover a waveform, however, we need to determine the corresponding phase information. As it turns out, a minimum-phase waveform is uniquely determined from the magnitude of its Fourier transform. In this section, we outline how we obtain an optimal waveform which is of minimum phase. To determine this waveform, we will use what is commonly referred to as the *Hilbert transform method*. This approach is originally due to Kolmogorov [9, 16] (see also pages 232–233 in [23]).

For each s, we seek a real-valued waveform $p(t, s)$ that is causal (i.e., zero for negative t) and whose Fourier transform $P(\omega, s)$ satisfies $W(\omega, s) = |P(\omega, s)|^2$. Because p is real-valued, its Fourier transform satisfies $P(-\omega, s) = \overline{P(\omega, s)}$.

The strategy is to extend the waveform spectrum to the complex ζ-plane so that $\omega = \mathrm{Re}\ \zeta$, $P(-\zeta, s) = \overline{P(\zeta, s)}$, and

$$W(\zeta, s) = P(-\zeta, s) P(\zeta, s), \tag{5.1}$$

where all singularities of $P(\zeta, s)$ lie in the upper half ζ-plane. Singularities of $P(\zeta, s)$ being only in the upper half-plane implies that $p(t, s)$ is causal.

We construct P as follows. For notational convenience, we omit the explicit functional dependence on s. Assuming for the moment that W is nonzero, we write

$$W(\zeta) = e^{\ln W(\zeta)} \qquad \text{and} \qquad P(\zeta) = e^{\ln P(\zeta)}. \tag{5.2}$$

For $\zeta = \omega$, where ω is real, $W(\omega) > 0$ is a real-valued, even function of ω, and therefore so is $\ln W(\zeta)$, which can therefore be written as

$$\ln W(\zeta) = C(-\zeta) + C(\zeta) \tag{5.3}$$

for some C whose singularities lie only in the upper half-plane. Therefore, (5.2) can be written as

$$W(\zeta) = e^{C(-\zeta) + C(\zeta)} = e^{C(-\zeta)} e^{C(\zeta)}, \tag{5.4}$$

which is of the desired form (5.1). By construction, the inverse Fourier transform $c(t)$ of $C(\zeta)$ is a causal function. Consequently we can take

$$P(\omega) = e^{C(\omega)}. \tag{5.5}$$

Strictly speaking, this method requires W to have a nonzero magnitude along the whole imaginary axis, as the logarithm is undefined at zero. To get around this problem, we regularize our spectrum slightly; first we consider a smoothed spectrum

$$W_\rho(\omega) := u_\rho \underset{\omega}{*} W(\omega), \tag{5.6}$$

where u_ρ is the heat kernel

$$u_\rho(\omega) := \frac{1}{\sqrt{2\pi\rho}} e^{-\omega^2/2\rho}. \tag{5.7}$$

The resulting W_ρ will be nonzero for all ω, and we can apply the above Hilbert-transform method to it and recover a waveform $p_\rho(t)$. Furthermore, $W_\rho(\omega)$ can be made arbitrarily close to $W(\omega, s)$ by choosing a small enough parameter ρ. The desired minimum-phase waveform $p(t)$ is then determined as a limit when ρ goes to zero:

$$p(t) = \lim_{\rho \to 0} p_\rho(t). \tag{5.8}$$

6. Numerical simulations. In this section we will numerically compute the optimal waveform for a particular scene. The scene which we want to image consists of two point scatterers which are embedded in a dispersive background. The point scatterers are placed symmetrically about the origin, 6 m apart, and the scattering is collected along a circular flight path with the center at the origin and a radius of 100 m. The antenna follows the flight path at a height of 10 m above the flat surface. Figure 2 outlines this scene.

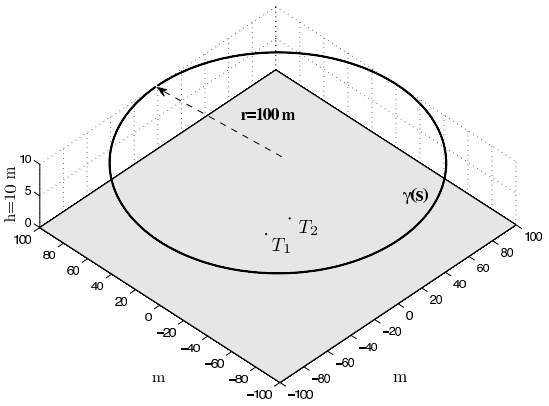

FIG. 2. *Imaging scenario: two point scatterers embedded in a dispersive background. The circular flight path has radius* 100 *m and is flown* 10 *m above the surface.*

We model the dispersive background using the Fung–Ulaby model for leafy vegetation. This model has two parameters: the leaf volume fraction and the water content volume fraction. Here we use $v_l = 0.04$ and $v_w = 0.2$ as the leaf and water

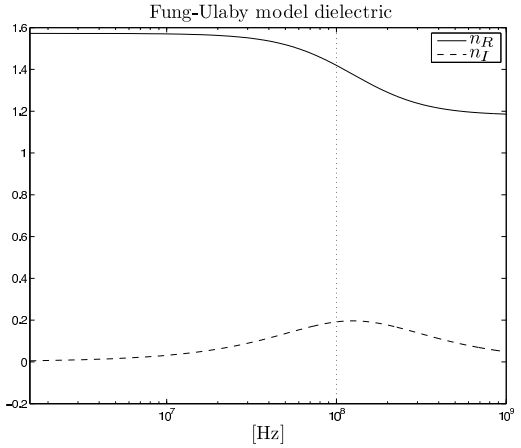

FIG. 3. *Profile of the real (solid) and imaginary (dashed) parts of the complex-valued refractive index with a time-relaxation parameter modeled according to the Fung–Ulaby model with relaxation time $\tau = 8$ ns. The leaf and water fraction parameters are $v_l = 0.04$ and $v_w = 0.2$, respectively. The vertical dotted line shows the center frequency of the transmitted waveform.*

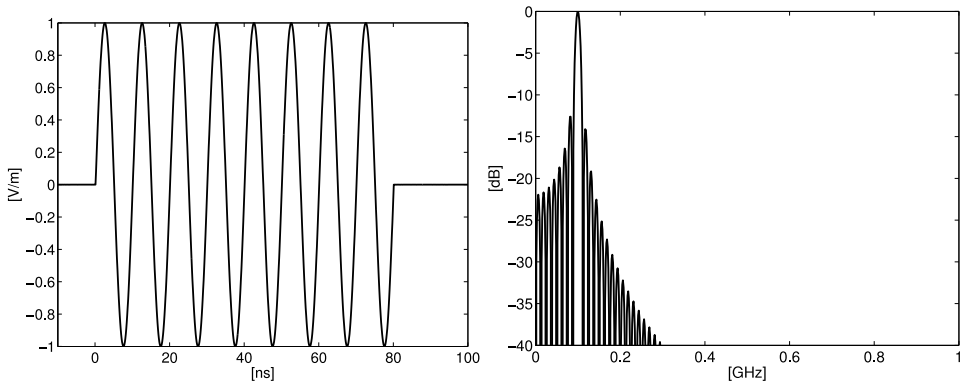

FIG. 4. *Unit-amplitude square pulse with 80 ns duration, modulated at 0.1 GHz, shown together with its spectrum (right). This waveform was used as a reference.*

fractions, respectively. Figure 3 shows the real and imaginary parts of the index of refraction for the background. The Fung–Ulaby model is detailed in Appendix B.

To simulate electronic receiver noise in the measurements, we added Gaussian white noise, independent for each antenna position around the flightpath. Furthermore, as in [30], we used a white target model for the point scatterers. In this situation, the noise-to-target ratio $\sigma_{\eta \mathrm{T}}$ is a constant. In [30] we showed that it is in fact closely related to the SNR for a unit-amplitude transmit waveform.

As a reference waveform we used a rectangular pulse with length 80 ns. This pulse was then multiplied by a carrier signal at 0.1 GHz to produce an 8-cycle sinusoid. The carrier frequency was chosen to correspond to a frequency in the middle of the band where the index of refraction of the background medium displays most deviations from a constant value. This transmit waveform, along with its frequency content, is shown in Figure 4.

In our simulations we use the 8-cycle sinusoid depicted in Figure 4, use (2.21) to

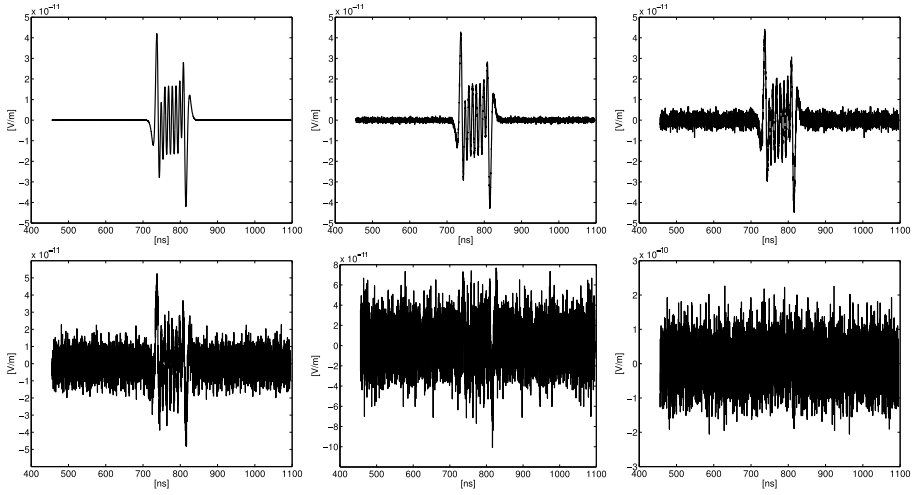

FIG. 5. *Scattering measurements for 8-cycle sinusoidal transmit waveform. These measurements have SNRs of* 40 *dB,* 20 *dB,* 10 *dB,* 0 *dB,* -10*dB, and* -20*dB, respectively.*

simulate the data, and then add noise so that the SNR of the simulated scattering is between 40 dB and -20dB. Samples of the simulated scattering measurements with different levels of additive noise are shown in Figure 5, where precursors can be seen as the large oscillations at the beginning and end of the main pulse.

The main constraint in the waveform design is that the transmit power should remain constant. The optimal waveform was computed to have the same transmit power as the 8-cycle sinusoid transmit waveform. This was accomplished by performing a bisection search for the correct value of λ for which the solution of (4.7) has the correct transmit power:

1. Choose an initial value of $\lambda > 0$.
2. Solve (4.8) to obtain $W(\omega) = |P(\omega)|^2$.
3. Compute the corresponding transmit power for $W(\omega)$.
4. If the transmit power is larger than that of the 8-cycle sinusoid, then increase λ. If the power is smaller, then decrease λ.
5. Repeat steps 2 to 4 until the transmit power is sufficiently close to that of the 8-cycle sinusoid.

We note that by symmetry of the simulated scenario, we may assume that the same waveform is transmitted at every point along the trajectory. The resulting waveform is therefore not a function of s.

Figure 6 shows the optimal waveforms for various levels of noise-to-target ratio. The corresponding frequency content is shown in Figure 7. We see that for low noise levels, it is optimal to transmit an extremely wideband waveform. However, as the noise level increases, the optimal waveform has most of its energy concentrated around 0.1 GHz. At the highest noise levels, we are left with what looks like only a few oscillations of a sinusoid.

In [20] the development of precursors was investigated. In particular, it was shown that a single-cycle sinusoid was an efficient way to generate precursors. As a second comparison, we therefore use a 1-cycle sinusoid as a waveform. This has much larger bandwidth than the 8-cycle sinusoid and should therefore be more comparable to the bandwidth of the optimal waveform. Figure 8 shows this waveform as well as its

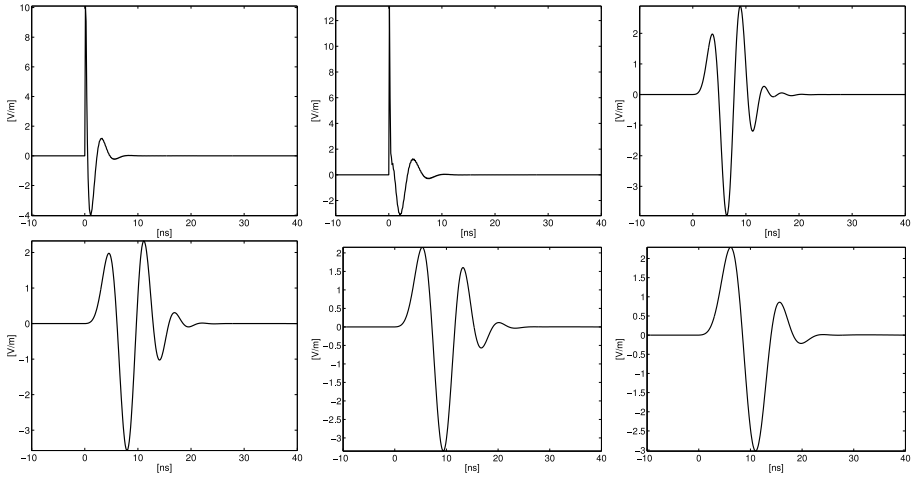

FIG. 6. *Optimal transmit waveform, as determined according to* (4.8)*, for varying levels of SNR:* 40*,* 20*,* 10*,* 0*,* −10*, and* −20*, respectively.*

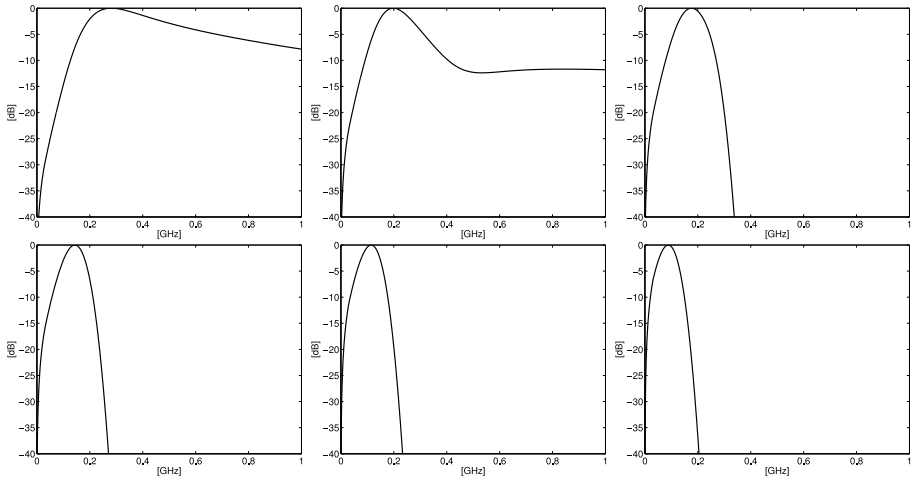

FIG. 7. *Frequency content of the optimal transmit waveforms in Figure* 6.

frequency content. In particular, we note that the main lobe of the spectrum has a width similar to that of the optimal waveform at high noise levels.

Figure 9 shows sample reconstructions using the 8-cycle sinusoid, the optimal waveform, and the 1-cycle sinusoid for various noise levels. As we can see, the extremely wideband optimal waveform gives very good results at low noise levels. At medium noise levels the optimal waveform still consistently produces a narrower peak width than the others. At high noise levels, the performance of the optimal waveform is closely matched by the 1-cycle sinusoid.

To better compare the reconstructions, we also plot cross sections along the straight line which goes through the correct target locations. This is shown in Figure 10. The narrower peak produced by the optimal waveform is clear from these plots when the noise level is moderate. For high noise levels, however, the 1-cycle sinusoid produces results similar to those of the optimal waveform.

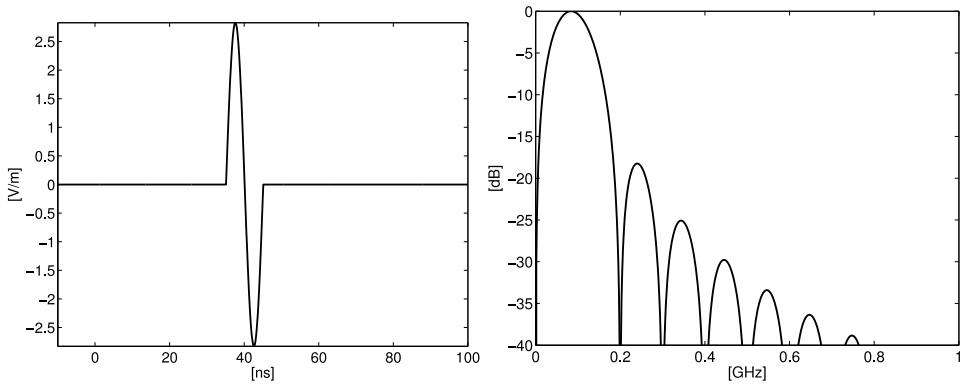

FIG. 8. 1-*cycle sinusoid generated from a* 10 *ns square pulse modulated at* 0.1 *GHz.*

Finally, we want to see how the different waveforms evolve with propagation distance. To do this, we simulate the propagation of a plane wave through the dispersive medium. Figure 11 shows the frequency spectrum evolving as we propagate forward in steps of 50 m. We note that the optimal waveform for low noise levels pumps a lot of energy into the frequencies above 0.1 GHz and thereby is able to maintain its broadband characteristics as it propagates. For high noise levels, however, the frequency spectrum resembles that of a precursor. In fact, when we get to the highest noise level, the frequency spectrum evolves as that of a pure precursor; the frequency spectrum does not undergo the initial transition where high-frequency content is dissipated quickly, as observed in the initial phase of the 1-cycle sinusoid.

7. Concluding remarks. In this paper we have derived a waveform which is designed to minimize the mean-square-error (MSE) in the reconstructed SAR image. Optimality is based on reconstruction being performed using a filtered backprojection reconstruction method which itself is optimal in the minimum MSE sense.

First, we derived the power spectrum of the optimal waveform as the solution of a nonlinear integral equation. We then derived an algorithmic approach to solving this equation. Finally, we obtained a unique optimal waveform by requiring the solution to be of minimum phase.

The analysis presented here is quite general and indicates that for low noise levels, or, equivalently, for large amounts of transmit power, the optimal waveform becomes an extremely broadband pulse. When the noise level is significant, however, the optimal waveform is strictly band-limited.

In the simulated results based on a Fung–Ulaby model for leafy vegetation, the ideal transmit spectrum is concentrated around the frequencies which are conducive to the generation of precursors. Indeed, we have shown that our optimal minimum-phase waveform closely resembles the precursor which is generated from a 1-cycle sinusoid. This suggests that under certain conditions, precursors may indeed be useful as transmit waveforms in SAR imaging.

Appendix A. Optimal reconstruction filter. This appendix provides a summary of the results in [30]. Because the target and the noise are statistically independent and have zero mean, the integral (3.3) can be split up as

$$\Delta(P,Q) = \int \langle |I(\boldsymbol{z}) - I_{\Omega_{\boldsymbol{z}}}(\boldsymbol{z})|^2 \rangle \mathrm{d}\boldsymbol{z} = \Delta_T(P,Q) + \Delta_\eta(P,Q), \tag{A.1}$$

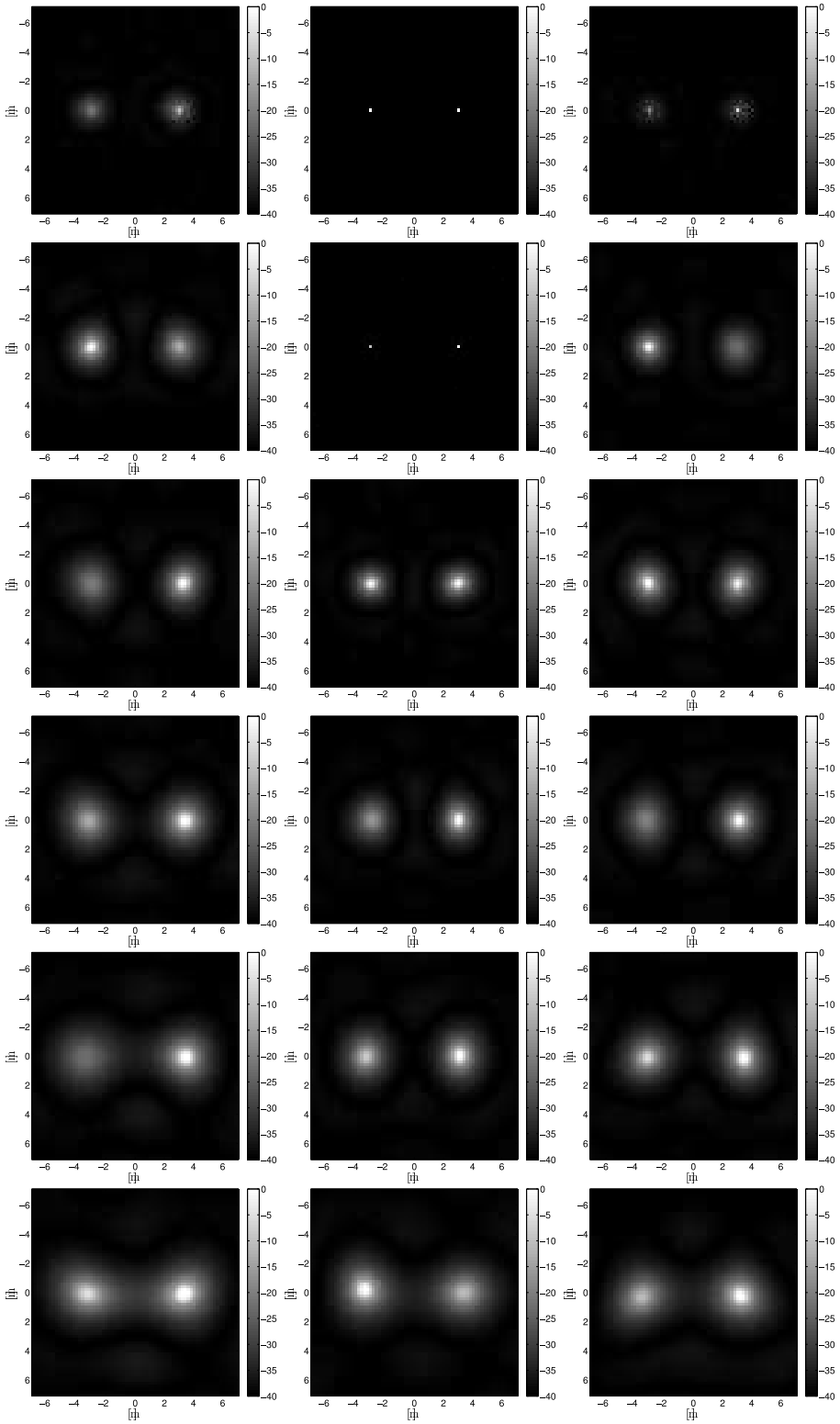

FIG. 9. *Reconstructions using* 8*-cycle sinusoid (left), optimal waveform (center), and* 1*-cycle sinusoid (right). The noise level increases from the top row to the bottom row.*

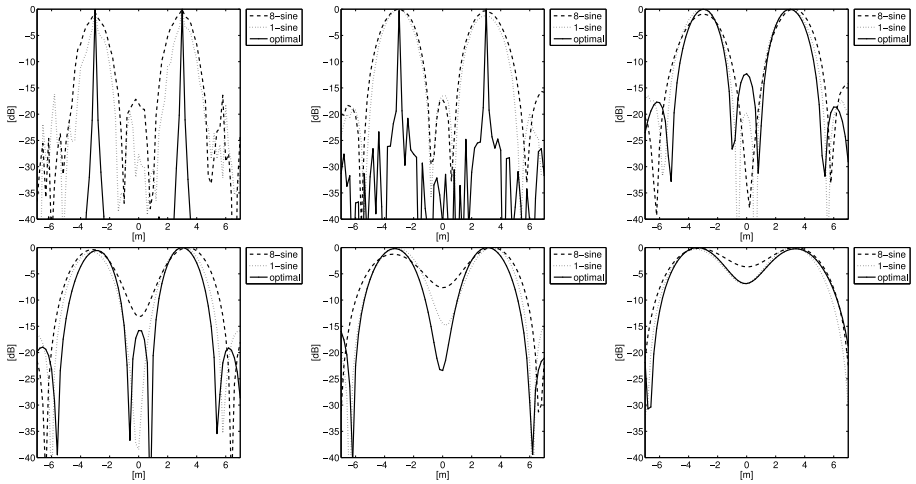

FIG. 10. *Cross sections of the reconstructed images.*

where

(A.2)
$$\Delta_T(P,Q) = \int \left\langle \left| \iint_{\Omega_{\boldsymbol{z}}} e^{i(\boldsymbol{z}-\boldsymbol{y})\cdot\boldsymbol{\xi}} Q(\boldsymbol{\xi},\boldsymbol{z}) A_P(\boldsymbol{\xi},\boldsymbol{y}) T(\boldsymbol{y}) J(\boldsymbol{\xi},\boldsymbol{z}) \mathrm{d}\boldsymbol{\xi}\mathrm{d}\boldsymbol{y} - I_{\Omega_{\boldsymbol{y}}}(\boldsymbol{z}) \right|^2 \right\rangle \mathrm{d}\boldsymbol{z},$$

and

$$\begin{aligned} \Delta_\eta(P,Q) = \Big\langle & \int e^{-i[\vartheta_R(\omega)|\mathbf{r}_{s,\boldsymbol{z}}|-\omega t]} Q(\omega,s,\boldsymbol{z}) \eta(t,s) \mathrm{d}t\mathrm{d}\omega\mathrm{d}s \\ & \times \int e^{i[\vartheta_R(\omega')|\mathbf{r}_{s',\boldsymbol{z}}|-\omega' t']} \overline{Q(\omega',s',\boldsymbol{z})\eta(t',s')} \mathrm{d}t'\mathrm{d}\omega'\mathrm{d}s' \Big\rangle \mathrm{d}\boldsymbol{z}. \end{aligned} \tag{A.3}$$

Here the bar denotes complex conjugate, $A_P(\boldsymbol{\xi},\boldsymbol{z}) = A(\boldsymbol{\xi},\boldsymbol{z})P(\boldsymbol{\xi})$, and $\boldsymbol{\xi}$ denotes the result of the Stolt change of variables

$$(\omega, s) \to \boldsymbol{\xi} = 2\omega n_R(\omega)\widehat{\mathbf{r}}_{s,\boldsymbol{z}}/c_0. \tag{A.4}$$

Expression (A.2) is the expected value of the inner product $(\mathcal{M}T, \mathcal{M}T)_{L^2} = (\mathcal{M}^*\mathcal{M}T, T)_{L^2}$, where $\mathcal{M}$ is the integral operator of (A.2), including the I_{Ω_z} term. Then $\mathcal{M}^*\mathcal{M}T$ can be written

$$\begin{aligned} [\mathcal{M}^*\mathcal{M}T](\boldsymbol{y}) &= \iint \iint_{\Omega_{\boldsymbol{z}}\times\Omega_{\boldsymbol{z}}} e^{i[(\boldsymbol{z}-\boldsymbol{y})\cdot\boldsymbol{\xi} - (\boldsymbol{z}-\boldsymbol{y}')\cdot\boldsymbol{\xi}']} \left[Q(\boldsymbol{\xi},\boldsymbol{z}) A_P(\boldsymbol{\xi},\boldsymbol{y}) J(\boldsymbol{\xi},\boldsymbol{z}) - 1\right] \\ &\quad \times \overline{\left[Q(\boldsymbol{\xi}',\boldsymbol{z}) A_P(\boldsymbol{\xi}',\boldsymbol{y}') J(\boldsymbol{\xi}',\boldsymbol{z}) - 1\right]} T(\boldsymbol{y}')\, \mathrm{d}\boldsymbol{\xi}\mathrm{d}\boldsymbol{\xi}'\mathrm{d}\boldsymbol{y}'\mathrm{d}\boldsymbol{z} \\ &= [(\mathcal{N}+\mathcal{L})T](\boldsymbol{y}), \end{aligned} \tag{A.5}$$

where we have applied the method of stationary phase in the variables $\boldsymbol{\xi}'$ and $\boldsymbol{z}$. Here $\mathcal{N}$ denotes the operator

$$\begin{aligned} \mathcal{N}T(\boldsymbol{y}) &= \iint_{\Omega_{\boldsymbol{y}}} e^{i[(\boldsymbol{y}'-\boldsymbol{y})\cdot\boldsymbol{\xi}]} \left[Q(\boldsymbol{\xi},\boldsymbol{y}') A_P(\boldsymbol{\xi},\boldsymbol{y}) J(\boldsymbol{\xi},\boldsymbol{y}') - 1\right] \\ &\quad \times \overline{\left[Q(\boldsymbol{\xi},\boldsymbol{y}') A_P(\boldsymbol{\xi},\boldsymbol{y}') J(\boldsymbol{\xi},\boldsymbol{y}') - 1\right]} T(\boldsymbol{y}')\, \mathrm{d}\boldsymbol{\xi}\mathrm{d}\boldsymbol{y}', \end{aligned} \tag{A.6}$$

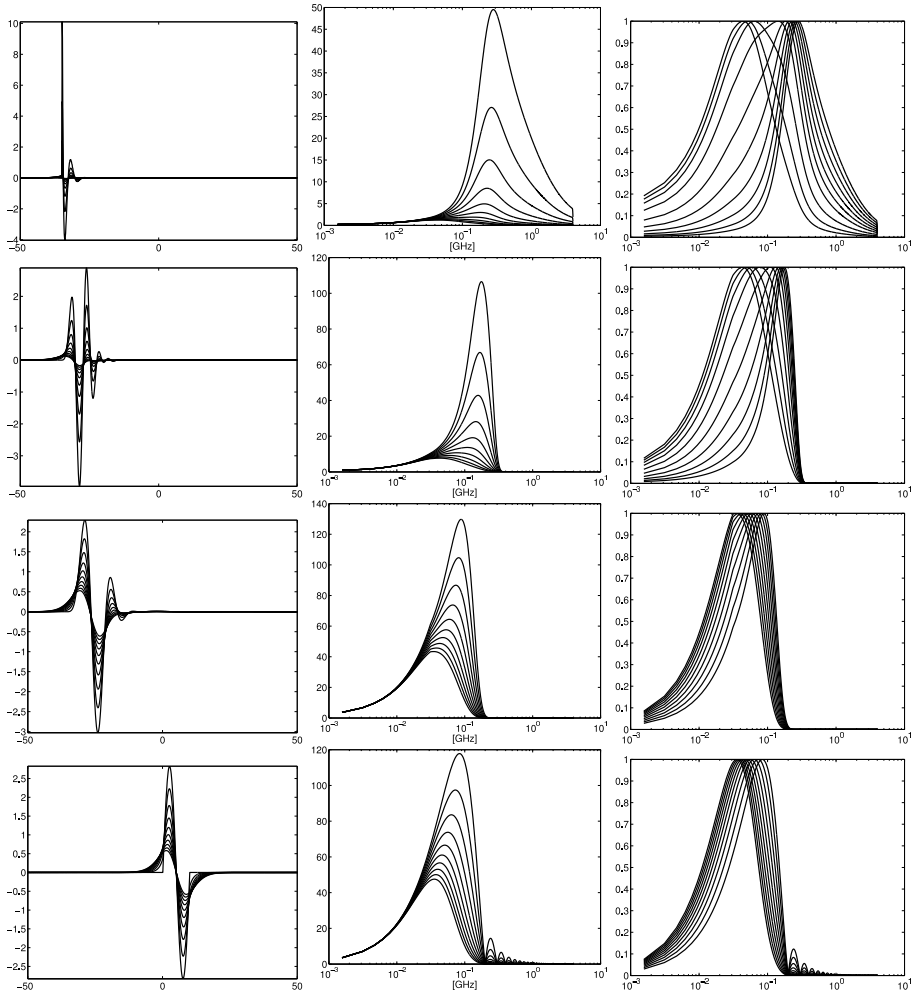

FIG. 11. *Propagating waveform (left column), evolving frequency spectrum (middle column), and normalized evolving frequency spectrum (right column). Top row: optimal waveform for lowest noise level. Second row: optimal waveform for medium noise level. Third column: optimal waveform for highest noise level. Bottom row:* 1*-cycle sinusoid.*

and $\mathcal{L}$ denotes an operator that, relative to $\mathcal{M}$, is smoothing. This follows because $\mathcal{M}^*\mathcal{M}$ is the composition of pseudodifferential operators [13, 28]. The expected value (A.2) can then be written

$$\Delta_T(P,Q) = \langle (NT,T)_{L^2} \rangle + \langle (LT,T)_{L^2} \rangle. \tag{A.7}$$

We neglect the second term of (A.7). In the first term, we bring the expectation inside the integral and use (3.6), thus obtaining

(A.8)

$$\Delta_T(P,Q) \approx \langle (NT,T)_{L^2} \rangle = \iint \iint_{\Omega_{\boldsymbol{y}}} e^{i[(\boldsymbol{y}'-\boldsymbol{y})\cdot(\boldsymbol{\xi}-\boldsymbol{\zeta})]} \left[Q(\boldsymbol{\xi},\boldsymbol{y}') A_P(\boldsymbol{\xi},\boldsymbol{y}) J(\boldsymbol{\xi},\boldsymbol{y}') - 1 \right]$$

$$\times \overline{[Q(\boldsymbol{\xi},\boldsymbol{y}') A_P(\boldsymbol{\xi},\boldsymbol{y}') J(\boldsymbol{\xi},\boldsymbol{y}') - 1]} S_T(\boldsymbol{\zeta}) \mathrm{d}\boldsymbol{\xi} \mathrm{d}\boldsymbol{\zeta} \mathrm{d}\boldsymbol{y} \mathrm{d}\boldsymbol{y}'.$$

Again we expect the main contributions to (A.8) to come from the region of the critical points $\boldsymbol{y} = \boldsymbol{y}'$ and $\boldsymbol{\xi} = \boldsymbol{\zeta}$. To see this, we introduce a large parameter by making the changes of variables $\boldsymbol{\xi} \to \lambda\boldsymbol{\xi}'$, where $|\boldsymbol{\xi}'| = 1$, and $\boldsymbol{\zeta} \to \lambda\boldsymbol{\zeta}'$, obtaining

$$\langle (NT,T)_{L^2} \rangle = \iint \iint_{\Omega_{\boldsymbol{y}}} e^{i\lambda[(\boldsymbol{y}'-\boldsymbol{y})\cdot(\boldsymbol{\xi}'-\boldsymbol{\zeta}')]} X(\lambda\boldsymbol{\xi}', \boldsymbol{y}', \boldsymbol{y}) S_T(\lambda\boldsymbol{\zeta}') \lambda^2 \mathrm{d}\boldsymbol{\xi}' \mathrm{d}\boldsymbol{\zeta}' \mathrm{d}\boldsymbol{y} \mathrm{d}\boldsymbol{y}', \tag{A.9}$$

where we have temporarily written

$$X(\boldsymbol{\xi}, \boldsymbol{y}, \boldsymbol{y}') := [Q(\boldsymbol{\xi}, \boldsymbol{y}') A_P(\boldsymbol{\xi}, \boldsymbol{y}) J(\boldsymbol{\xi}, \boldsymbol{y}') - 1] \, \overline{[Q(\boldsymbol{\xi}, \boldsymbol{y}') A_P(\boldsymbol{\xi}, \boldsymbol{y}') J(\boldsymbol{\xi}, \boldsymbol{y}') - 1]}. \tag{A.10}$$

Applying the method of stationary phase in the $\boldsymbol{\zeta}'$ and $\boldsymbol{y}'$ variables and then undoing the change of variables results in

$$\langle (NT,T)_{L^2} \rangle \propto \iint [X(\boldsymbol{\xi}, \boldsymbol{y}, \boldsymbol{y}) S_T(\boldsymbol{\xi}) + R(\boldsymbol{\xi}, \boldsymbol{y})] d\boldsymbol{\xi} d\boldsymbol{y}, \tag{A.11}$$

where the remainder term R decays more rapidly in $\lambda = |\boldsymbol{\xi}| = 2\omega n_R(\omega)/c_0$ than the first term. For radar systems in which ω/c_0 is large, therefore, the remainder term is expected to be small, and we neglect it.

With these approximations, we have

$$\Delta_T(P,Q) \approx \int \int_{\Omega_{\boldsymbol{y}}} |Q(\boldsymbol{\xi}, \boldsymbol{y}) A_P(\boldsymbol{\xi}, \boldsymbol{y}) J(\boldsymbol{\xi}, \boldsymbol{y}) - 1|^2 \, S_T(\boldsymbol{\xi}) d\boldsymbol{\xi} \mathrm{d}\boldsymbol{y}. \tag{A.12}$$

We now revert to the original coordinates $\boldsymbol{\xi} \to (\omega, s)$; by undoing the Stolt change of variables in (A.12) we get

$$\Delta_T(P,Q) \approx \iiint |Q(\omega, s, \boldsymbol{y}) A_P(\omega, s, \boldsymbol{y}) J(\omega, s, \boldsymbol{y}) - 1|^2 \, S_T(\boldsymbol{\zeta}(\omega, s, \boldsymbol{y})) \frac{\mathrm{d}\omega \mathrm{d}s}{J(\omega, s, \boldsymbol{y})} \mathrm{d}\boldsymbol{y}. \tag{A.13}$$

Rearranging (A.3) we obtain

$$\begin{aligned} \Delta_\eta(P,Q) &= \iiint \iiint e^{-i[\vartheta_R(\omega)|\mathbf{r}_{s,\boldsymbol{y}}| - \vartheta_R(\omega')|\mathbf{r}_{s',\boldsymbol{y}}|]} Q(\omega, s, \boldsymbol{y}) \overline{Q(\omega', s', \boldsymbol{y})} \\ &\qquad \times \int e^{-i\omega t} e^{i'\omega t'} \langle \eta(t,s) \overline{\eta(t',s')} \rangle \mathrm{d}t' dt \mathrm{d}\omega' \mathrm{d}s' \mathrm{d}\omega \mathrm{d}s \mathrm{d}\boldsymbol{y} \end{aligned} \tag{A.14}$$

$$= \iiint |Q(\omega, s, \boldsymbol{y})|^2 S_\eta(\omega, s) \mathrm{d}\omega \mathrm{d}s \mathrm{d}\boldsymbol{y}, \tag{A.15}$$

where we have used the noise properties (3.7) in (A.14).

Combining (A.13) and (A.14) we get the following integral expression for the variance in the reconstruction:

$$\Delta(P,Q) \approx \iiint |Q(\omega, s, \boldsymbol{y}) A_P(\omega, s, \boldsymbol{y}) J(\omega, s, \boldsymbol{y}) - 1|^2 \, \frac{S_T(\boldsymbol{\xi}(\omega, s, \boldsymbol{y}))}{J(\omega, s, \boldsymbol{y})} \mathrm{d}\omega \mathrm{d}s \mathrm{d}\boldsymbol{z} \tag{A.16a}$$

$$+ \iiint |Q(\omega, s, \boldsymbol{y})|^2 S_\eta(\omega, s) \mathrm{d}\omega \mathrm{d}s \mathrm{d}\boldsymbol{y}. \tag{A.16b}$$

In order to find the optimal filter $Q = Q^{\mathrm{opt}}$ for which (3.14) is minimized, we set to zero the variational derivative of $\Delta(P,Q)$ with respect to Q and obtain [30] the equation

$$\left(|A_P|^2 Q^{\mathrm{opt}} J - \overline{A_P} \right) S_T + Q^{\mathrm{opt}} S_\eta = 0. \tag{A.17}$$

Solving for Q^{opt} we find that

$$Q^{\text{opt}}(\omega, s, \boldsymbol{y}) = \frac{\overline{A_P(\omega, s, \boldsymbol{y})}}{|A_P(\omega, s, \boldsymbol{y})|^2 J(\omega, s, \boldsymbol{y}) + S_\eta(\omega, s)/S_T(\boldsymbol{\xi}(\omega, s, \boldsymbol{y}))}. \tag{A.18}$$

Finally, we substitute back $A_P(\omega, s, \boldsymbol{y}) = A(\omega, s, \boldsymbol{y})P(\omega, s)$. We summarize this result in the following theorem.

THEOREM A.1 (optimal reconstruction filter). *Let the background medium satisfy Assumption* 2.1. *Let the stochastic target model satisfy Assumption* 3.1. *In* (3.1)*, the filter Q that is optimal, in the sense of minimizing the variance* (3.14) *in the leading-order contributions of the image, is approximated by*

$$Q^{\text{opt}}(\omega, s, \boldsymbol{y}) = \frac{\overline{A(\omega, s, \boldsymbol{y})P(\omega)}}{|A(\omega, s, \boldsymbol{y})P(\omega)|^2 J(\omega, s, \boldsymbol{y}) + \sigma_{\eta T}(\omega, s)}, \tag{A.19}$$

where the (frequency-domain) noise-to-target ratio $\sigma_{\eta T}$ is defined as

$$\sigma_{\eta T}(\omega, s, \boldsymbol{y}) := S_\eta(\omega, s)/S_T(\omega, s, \boldsymbol{y}), \tag{A.20}$$

and we have used (A.4) *to define $S_T(\omega, s, \boldsymbol{y})$,*

$$S_T(\omega, s, \boldsymbol{y}) := S_T(\,\xi(\omega), s, \boldsymbol{y}\,), \tag{A.21}$$

and A is given by (3.9).

Appendix B. The Fung–Ulaby model. In our numerical examples, we used the model for complex-valued permittivity developed by Fung and Ulaby [11] for vegetation. In this model, the permittivity of the vegetation (taken to be a combination of water and some solid material) was estimated by a mixing formula for two-phase mixtures [10, 29]. The effective relative permittivity is given by

$$\epsilon_{r,\text{eff}}(\omega) = v_l \epsilon_l + (1 - v_l), \tag{B.1}$$

where $\epsilon_l = \epsilon_R(\omega) + i\,\epsilon_I(\omega)$, and

$$\epsilon_R(\omega) = 5.5 + \frac{e_m - 5.5}{1 + \tau^2\omega^2},$$
$$\epsilon_I(\omega) = \frac{(e_m - 5.5)\tau\omega}{1 + \tau^2\omega^2},$$

where $e_m = 5 + 51.56 v_w$, where v_l is the fractional volume occupied by leaves, v_w is the water volume fraction within a "typical leaf," and τ is an empirical relaxation time of water molecules. The relaxation time τ is governed by the interaction of the water molecules with their environment and by the temperature T. The relaxation time for pure water at 20 °C is $\tau \approx 10.1 \times 10^{-12}$ s.

REFERENCES

[1] D. BLACK, *An overview of impulse radar phenomenon*, IEEE AES Systems Magazine, 7 (1992), pp. 6–11.

[2] N. BLEISTEIN, J. K. COHEN, AND J. W. STOCKWELL, *The Mathematics of Multidimensional Seismic Inversion*, Springer, New York, 2000.

[3] L. BRILLOUIN, *Wave Propagation and Group Velocity*, Academic Press, New York, 1960.

[4] N. A. Cartwright and K. E. Oughstun, *Uniform asymptotics applied to ultrawideband pulse propagation*, SIAM Rev., 49 (2007), pp. 628–648.
[5] M. Cheney and B. Borden, *Problems in synthetic-aperture radar imaging*, Inverse Problems, 25 (2009), 123005.
[6] M. Cheney, D. Isaacson, and M. Lassas, *Optimal acoustic measurements*, SIAM J. Appl. Math., 61 (2001), pp. 1628–1647.
[7] M. Cheney and G. Kristensson, *Optimal electromagnetic measurements*, J. Electromagn. Waves Appl., 15 (2001), pp. 1323–1336.
[8] M. Cheney and C. J. Nolan, *Synthetic-aperture imaging through a dispersive layer*, Inverse Problems, 20 (2004), pp. 507–532.
[9] J. F. Claerbout, *Fundamentals of Geophysical Data Processing*, McGraw–Hill, New York, 1976.
[10] M. A. El-Rayes and F. T. Ulaby, *Microwave dielectric spectrum of vegetation—part* I: *Experimental observations*, IEEE Trans. Geosci. Remote Sensing, 25 (1987), pp. 541–549.
[11] A. K. Fung and F. T. Ulaby, *A scatter model for leafy vegetation*, IEEE Trans. Geosci. Electron., 16 (1978), pp. 281–286.
[12] W. Greiner, *Classical Electrodynamics*, Springer, New York, 1998.
[13] A. Grigis and J. Sjöstrand, *Microlocal Analysis for Differential Operators*, London Math. Soc. Lecture Note Ser. 196, Cambridge University Press, Cambridge, UK, 1994.
[14] J. D. Jackson, *Classical Electrodynamics*, 3rd ed., John Wiley & Sons, New York, 1999.
[15] G. M. Jenkins and D. G. Watts, *Spectral Analysis and Its Applications*, Holden-Day, San Francisco, 1968.
[16] A. Kolmogorov, *Sur l'interpolation et l'extrapolation des suites stationaires*, C. R. Acad. Sci., 208 (1939), pp. 2043–2045.
[17] G. Kristensson, *Direct and inverse scattering problems in dispersive media—Green's functions and invariant imbedding techniques*, in Methoden und Verfahren der Mathematischen Physik 37, Peter Lang, Frankfurt am Main, Germany, 1991.
[18] D. Lukofsky, J. Bessette, H. Jeong, E. Garmire, and U. Osterberg, *Can precursors improve the transmission of energy at optical frequencies?*, J. Modern. Opt., 56 (2009), pp. 1083–1090.
[19] P. W. Milonni, *Fast Light, Slow Light and Left-Handed Light*, Ser. Opt. Optoelectron., Institute of Physics, Bristol, UK, 2005.
[20] K. E. Oughstun, *Dynamical evolution of the Brillouin precursor in Rocard-Powles-Debye model dielectrics*, IEEE Trans. Antennas and Propagation, 53 (2005), pp. 1582–1590.
[21] K. E. Oughstun and G. C. Sherman, *Electromagnetic Pulse Propagation in Causal Dielectrics*, Springer-Verlag, Berlin, 1994.
[22] A. Papoulis, *The Fourier Integral and Its Applications*, McGraw–Hill, New York, 1962.
[23] A. Papoulis, *Signal Processing*, McGraw–Hill, New York, 1977.
[24] T. M. Roberts, *Radiated pulses decay exponentially in materials in the far fields of antennas*, Electron. Lett., 38 (2002), pp. 679–680.
[25] A. Sihvola, *Electromagnetic Mixing Formulas and Applications*, The Institution of Electrical Engineers, London, 1999.
[26] M. I. Skolnik, *Introduction to Radar Systems*, McGraw–Hill, NY, 1962.
[27] M. Stein, *Interpolation of Spatial Data*, Springer-Verlag, New York, 1999.
[28] F. Treves, *Introduction to Pseudodifferential and Fourier Integral Operators, Vols.* I–II, Plenum Press, New York, 1980.
[29] F. T. Ulaby and M. A. El-Rayes, *Microwave dielectric spectrum of vegetation—part* II: *Dual-dispersion model*, IEEE Trans. Geosci. Remote Sensing, 25 (1987), pp. 550–557.
[30] T. Varslot, J. H. Morales, and M. Cheney, *Synthetic-aperture radar imaging through dispersive media*, Inverse Problems, 26 (2010), 025008.
[31] T. Varslot, C. E. Yarman, M. Cheney, and B. Yazici, *A variational approach to waveform design for synthetic-aperture imaging*, Inverse Probl. Imaging, 1 (2007), pp. 577–592.
[32] B. Yazici, M. Cheney, and C. E. Yarman, *Synthetic aperture inversion for an arbitrary flight trajectory in the presence of noise and clutter*, Inverse Problems, 22 (2006), pp. 1705–1729.